remote sensing

MDPI

Article

Coastal Upwelling Front Detection off Central Chile (36.5–37°S) and Spatio-Temporal Variability of Frontal Characteristics

Vera Oerder [1,*], Joaquim P. Bento [2,3], Carmen E. Morales [1,4], Samuel Hormazabal [1,2] and Oscar Pizarro [1,5]

1 Millennium Institute of Oceanography (IMO), University of Concepcion, P.O. Box 1313, Concepción-3, Concepción 4030000, Chile; camorale@udec.cl (C.E.M.); samuel.hormazabal@ucv.cl (S.H.); orpa@profc.udec.cl (O.P.)
2 Escuela de Ciencias del Mar, Pontificia Universidad Católica de Valparaíso (PUCV), Casilla 1020, Valparaíso 2340000, Chile; jnettojunior@gmail.com
3 Institute of Oceanography, University of Hamburg, 20146 Hamburg, Germany
4 Depto. Oceanografía, Facultad de Ciencias Naturales y Oceanográficas, Universidad de Concepción (UdeC), Casilla 160-C, Concepción-3, Concepción 4030000, Chile
5 Depto. Geofísica, Facultad de Ciencias Físicas y Matemáticas, Universidad de Concepción (UdeC), Casilla 160-C, Concepción-3, Concepción 4030000, Chile
* Correspondence: vera.oerder@imo-chile.cl; Tel.: +56-412-203-742

Received: 13 March 2018; Accepted: 25 April 2018; Published: 30 April 2018

check for updates

Abstract: In Eastern Boundary Upwelling Systems, cold coastal waters are separated from offshore by a strong cross-shore Sea Surface Temperature (SST) gradient zone. This upwelling front plays a major role for the coastal ecosystem. This paper proposes a method to automatically identify the front and define its main characteristics (position, width, and intensity) from high resolution data. The spatio-temporal variability of the front characteristics is then analyzed in a region off Central Chile (37°S), from 2003 to 2016. The front is defined on daily 1 km-resolution SST maps by isotherm T_0 with T_0 computed from mean SST with respect to the distance from the coast. The probability of detecting a front, as well as the front width and intensity are driven by coastal wind conditions and increased over the 2007–2016 period compared to the 2003–2006 period. The front position, highly variable, is related to the coastal jet configuration and does not depend on the atmospheric forcing. This study shows an increase by 14% in the probability of detecting a front and also an intensification by 17% of the cross-front SST difference over the last 14 years. No trend was found in the front position.

Keywords: Eastern Boundary Upwelling System; coastal upwelling front detection; upwelling spatio-temporal variability; climate change

1. Introduction

In the main Eastern Boundary Current Systems (EBUS: California, Humboldt, Canarias, and Benguela), upwelling forced by alongshore equatorward winds usually creates a surface cold tongue in the coastal band. This cold tongue is limited offshore by a strong cross-shore density gradient zone, referred to as the upwelling front (e.g., [1–4]). Such front separates the nutrient-rich shelf waters nearshore from the lower nutrient water masses in the oceanic area or Coastal Transition Zone (CTZ) (e.g., [5–7]). In addition, this front acts as a retention and accumulation zone, and usually represents a barrier for the offshore distribution of coastal planktonic components [8–11]. Altogether, upwelling dynamics and retention of coastal waters are important processes in the understanding of the dispersal of coastal waters, nutrients and plankton and, thus, the dynamics of EBUS.

The upwelling cold tongue frequently presents strong seasonality in association with the annual cycle of upwelling-favorable winds and it can be easily observed from high resolution satellite Sea Surface Temperature (SST) distribution (e.g., [12,13]). However, the upwelling front characteristics (i.e., position, magnitude and width) and their spatio-temporal variability have been infrequently documented for the main EBUS, especially at the high frequency scales of variability. Studies of upwelling fronts using time-averaged SST maps underestimate the SST gradients intensity. For example, off Central Chile, the SST gradient intensity over the front computed from seasonal means was found to be $\sim$0.01 °C km^{-1}, whereas weekly SST gradients can be one order of magnitude higher, $\sim$0.1–0.25 °C km^{-1} [7].

Mesoscale and submesoscale structures (i.e., eddies, filaments, and meanders), common in EBUS, also contribute to create additional SST gradients in the CTZ. They are here referred as secondary fronts as opposed to the main upwelling front. In the early stages of their development, some of these structures have been observed interacting with the main upwelling front [6,7] and allowing cross-shore exchanges of coastal and oceanic diatom species [14]. In such cases, the upwelling front is locally deformed by the mesoscale or submesoscale feature.

Several methods have been developed that can automatically identify fronts from SST maps (e.g., [15–18]). Most of them are based on the detection of horizontal gradients in satellite SST (e.g., [19,20]) or on the statistical analysis of the SST distribution (e.g., [16,21–23]). Statistical methods assess whether a temperature threshold can be defined to separate the SST distribution into two distinct classes. When this condition is fulfilled, the isotherm corresponding to the threshold temperature defines the front in the SST map. Such methods are designed to identify all kinds of SST fronts in a given region and not specifically the main upwelling front. Previous studies in the upwelling region off Central Chile have used a fixed isotherm to define the upwelling front [7,14]. However, this has limitations because this value is likely to vary in time, especially under strong seasonality in upwelling at mid-latitudes. Thus, a new method is required to automatically determine for each SST map the most adequate isotherm defining the main upwelling front in EBUS.

Here, we focus on the upwelling front in a mid-latitude region of the Humboldt Current System (HCS), in the area off Point Lavapie (36.5–37°S, Central Chile). In the HCS, SST is affected by both the wind-induced upwelling and the heat fluxes at the air-sea interface (e.g., [24–27]). The propagation of coastal-trapped waves (CTW) also plays a role in the SST variability [24,28], in particular during El Niño Southern Oscillation (ENSO) events [29,30]. The imprint of CTWs is strong in the Northern HCS, but off Central Chile (30–40°S) their amplitude is largely attenuated so that the SST can be inferred from a one-dimensional model forced by the local wind stress and solar heating [24]. The region off Central-South Chile (35–40°S) is characterized by a strong seasonality in the coastal wind stress and the wind stress curl, with upwelling-favorable wind conditions from September to April (e.g., [13,31]). The upwelling-induced coastal cold tongue is present from November to May, suggesting a lag in the seasonal response of the SST to the wind conditions [13]. This delay has been explained by the concurrent effects of increasing solar heating and upwelling-favorable wind, which result in a warming of the surface layer and a cooling in the 20–80 m layer during austral spring Indeed, the temperature difference between the surface and 80 m depth is only $\sim$1–2 °C during this season, indicating that the effect of the upwelling on the SST is low. During summer and fall, the water column stratification increases (up to $\sim$4 °C difference between the same layers) and even weak upwelling events can strongly affect the SST [13].

In central-southern Chile, Point Lavapie (37°S) has been recognized as a main upwelling center [32]. This location has also been associated with the formation of an offshore meander of the coastal equatorward jet and of recurrent mesoscale features [7,31–33]. Studying a few cases in this area, Letelier et al. [7] suggested that the upwelling front position corresponds to that of the coastal jet meander. Just north of Point Lavapie, relative high mean frontal probabilities and an enhancement of frontal activity over the shelf and up to 200 km offshore have been observed [34]. In this area, the characteristics of the main upwelling front and their frequency of variability remain poorly described. This issue is nevertheless of high relevance in terms of the front influence on coastal planktonic communities and their contribution to high primary production levels, which support particularly large fish landings in this area [35].

The objective of this paper is first to propose a new method for the automatic detection of the main upwelling front using high resolution SST maps in EBUS. This method is then applied to describe and understand the variability of the front characteristics (probability of detecting a front, magnitude, and position) in a small area off Point Lavapie. The extent to which this variability can be related to local atmospheric forcing and oceanic circulation is also explored. The front characteristics are analyzed in Section 3, before the results are discussed in Section 4. Finally, we conclude in Section 5.

2. Materials and Methods

2.1. Observational Datasets

To detect the main upwelling front, the Group for High Resolution Sea Surface Temperature (GHRSST) Multi-scale Ultra-high Resolution (MUR) SST dataset [36] is used. MUR is a merged product of satellite and in situ observations from the NASA Advanced Microwave Scanning Radiometer-EOS (AMSRE), the Moderate Resolution Imaging Spectroradiometer (MODIS), the US Navy microwave WindSat radiometer, the Advanced Very High Resolution Radiometer (AVHRR), and in situ SST observations from the NOAA iQuam project. This dataset provides daily SST maps with 1 km resolution from 2003 to 2016.

During the PHYTO-FRONT short-term ship survey [14], two cross-shore transects (36.75°S and 36.5°S) were carried out during early February 2014. The shallowest CTD temperature measures (3.5 m depth) are used here to compare the upwelling front identified using in situ data and MUR SST.

The oceanic circulation is studied using surface geostrophic velocities computed from SSALTO/DUACS Sea Surface Height (SSH) satellite observations [37] distributed by the Copernicus Marine Environment Monitoring Service (CMEMS). Previously distributed by Aviso+, this product merges data from all altimeter missions: Jason-3, Sentinel-3A, HY-2A, Saral/AltiKa, Cryosat-2, Jason-2, Jason-1, T/P, ENVISAT, GFO, and ERS1. The L4 version provides daily SSH anomaly maps with 25 km resolution from 2003 to 2016 that allows us to study the coastal jet meanders with respect to its mean position. Coastal jets are defined here by alongshore velocities V_{along} above 0.1 m s^{-1} within 300 km nearshore. Consecutive pixels presenting such values of V_{along} are considered part of the same coastal jet. Two pixels with $V_{along} > 0.1$ m s^{-1} and separated by at least one pixel with $V_{along} \leqslant 0.1$ m s^{-1} are considered part of two different jets. All daily maps are analyzed and classified according to the number of coastal jets detected in the area.

Coastal wind stress conditions can be inferred from scatterometer observations. The 2003–2016 period was continuously monitored by several instruments deployed over different periods. However, when analyzing raw data, differences among the missions calibrations introduce bias in the wind stress tendency [38]. To solve this issue, wind data from sparse scatterometer fields (ERS, QuikSCAT, and ASCAT) have been processed by the IFREMER and compared to other data sources, such as radiometer data (SSM/I) and atmospheric wind reanalyses (ERA-Interim), to produce a new long time wind product described by Desbiolles et al. [39]. This dataset provides 6 h wind stress maps at 1/4° spatial resolution over the 2003–2016 period. To avoid data contamination by the land–ocean transition, the upwelling-favorable wind conditions are estimated here by averaging the daily alongshore wind stress intensity between 75 and 150 km from the coast and from 37 to 36.5°S.

Short-wave heat forcing at the air-sea interface is studied using the National Oceanography Centre Southampton (NOCS) Version 2.0 Surface Flux Dataset [40] over the 2003–2014 period. NOCS surface fluxes are computed from daily fields of the surface meteorological parameters (ICOADS Release 2.4 ship data for the years 2003–2006, and ICOADS Release 2.5 for the years 2007–2014) using bulk parameterizations [41]. The released dataset provides monthly mean values with a 1° resolution. Short-wave heat flux conditions are estimated here by averaging the solar heat flux over the 300 km nearshore (area used to detect and analyze the upwelling front; see Section 2.2).

2.2. Upwelling Front Detection Method

2.2.1. General Methodology

Here, the presence of an upwelling front is detected from the SST daily maps on a reduced latitude range (0.5°). The methodology, described in the following, is divided into two steps: In Section 2.2.2, a "frontal zone" (i.e, the zone with high mean cross-shore SST gradient) is first detected. The upwelling front is defined afterwards as the isotherm corresponding to the mean SST over the frontal zone. Then, in Section 2.2.3, the front characteristics are computed from the alongshore mean SST in the frontal zone. Figure 1 shows some examples of front detections. The presence of intense and large mesoscale structures can sometimes create a mean cross-shore SST gradient outside the frontal zone and of comparable intensity (Figure 1b). In such cases, which represent ∼30% of the maps, both the main frontal zone and this secondary frontal zone are identified. The method is summarized on Figure 2.

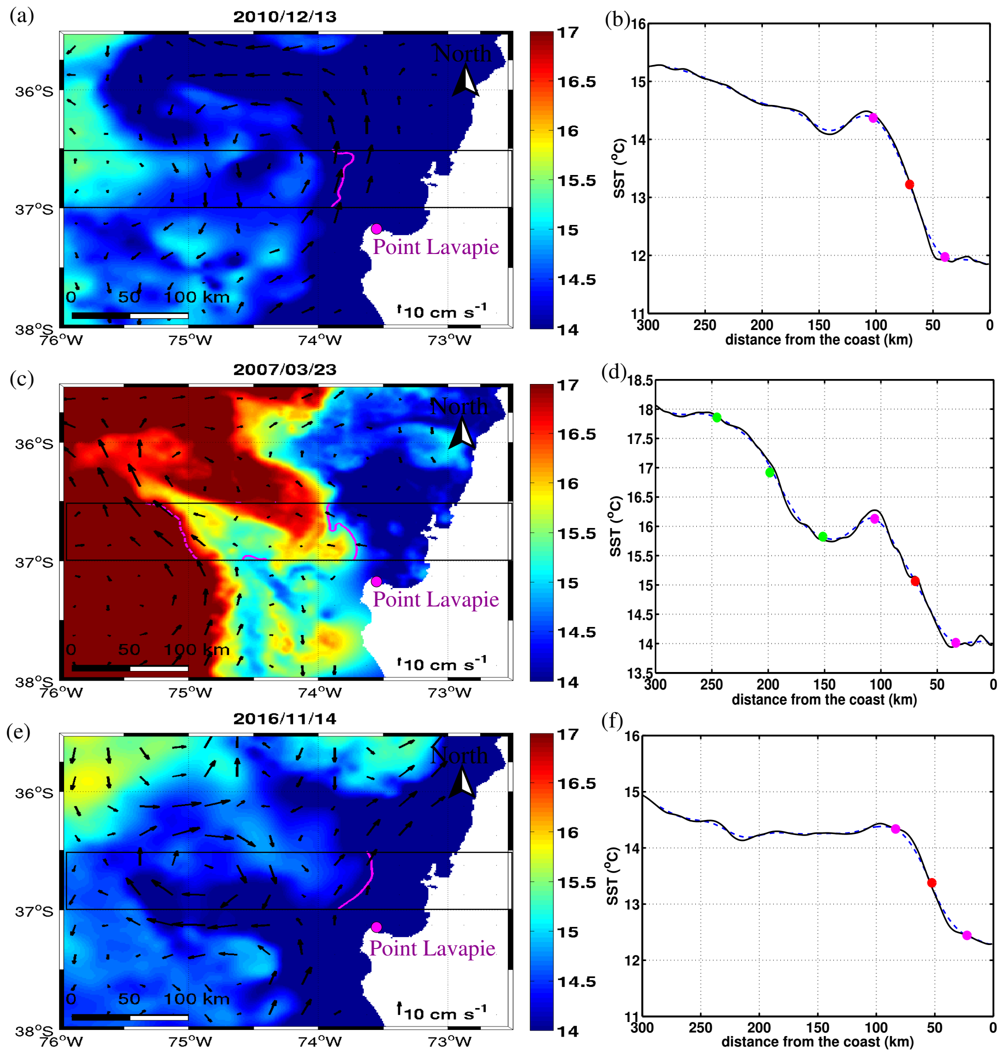

Figure 1. Daily SST (colors, in °C) observations and geostrophic currents (arrows) derived from SSH observations for: (**a**) 13 December 2010; (**c**) 24 March 2007; and (**e**) 14 November 2016. Black box indicates the studied area and the main (secondary) upwelling front is marked with plain (dotted, respectively) magenta line. Magenta dot indicates Point Lavapie. Mean daily SST (in °C, averaged over the studied latitude range) with respect to the distance from the coast (black line) for: (**b**) 13 December 2010; (**d**) 24 March 2007; and (**f**) 14 November 2016. Dotted blue line represents the smoothed mean SST and magenta (red) circles mark the extremity (center, respectively) of the main frontal zone. Green circles mark the secondary frontal zone extremities and center.

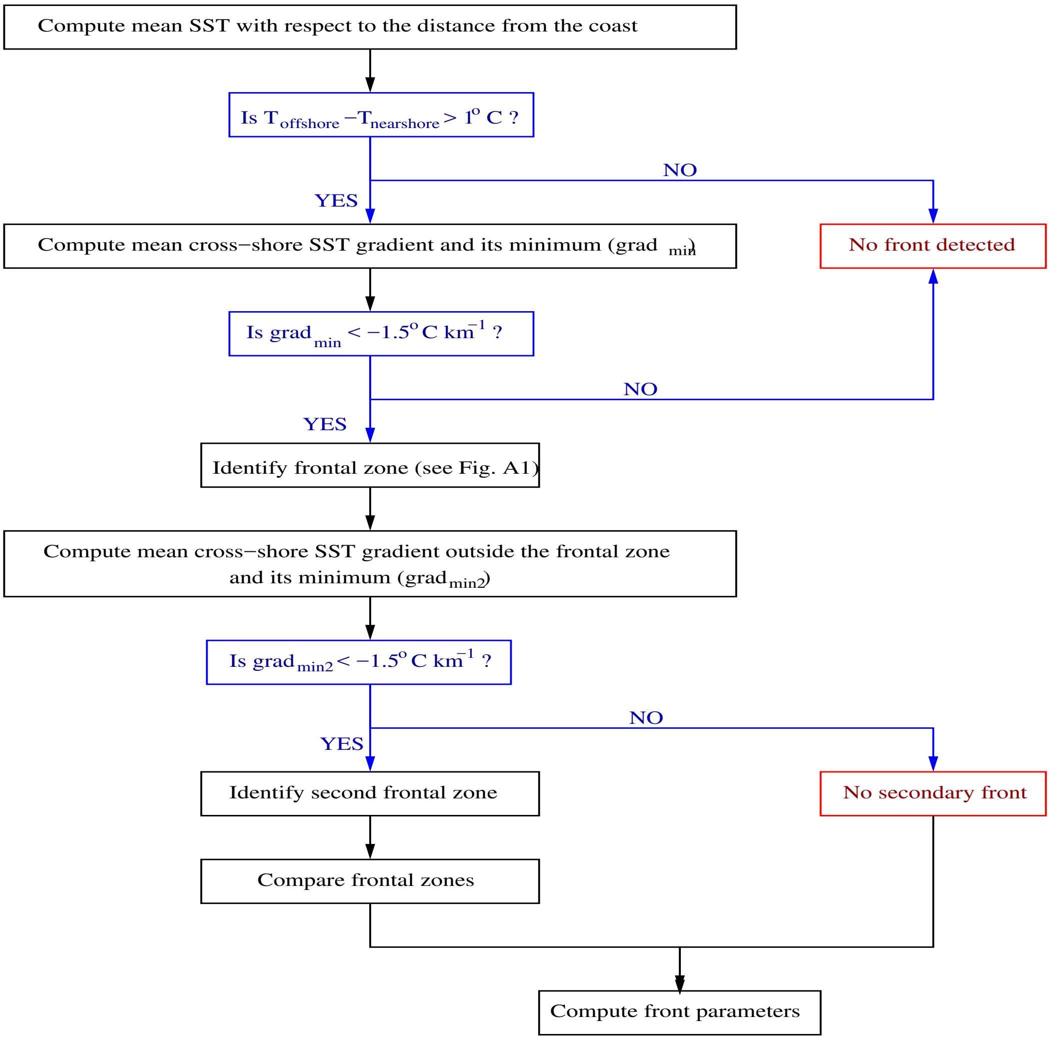

Figure 2. Scheme of the general front detection method.

2.2.2. Front Detection

To identify the frontal zone, SST are latitude-averaged in the 300 km nearshore to compute the mean SST with respect to the distance from the coast (Figure 1). The mean SST at 1 km ($T_{nearshore}$) and at 300 km ($T_{offshore}$) from the coast are computed. When the difference $T_{offshore} - T_{nearshore}$ is below 1 °C, we consider that there is no upwelling, and, thus no upwelling front is detected. When $T_{offshore} - T_{nearshore}$ is stronger than 1 °C, the mean SST is smoothed using a 30 km running mean. The goal of the latitude average and the cross-shore smoothing is to filter small scales variations associated with mesoscale structures. The smoothed SST is derived to compute the cross-shore SST gradient ($grad$) and its minimum ($grad_{min}$). $grad_{min}$ values are always negative because $T_{nearshore} < T_{offshore}$. We consider that there is no upwelling front that can be detected when $grad_{min}$ is weak ($grad_{min} \geqslant grad_{LIM}$ with $grad_{LIM} = -1.5 \times 10^{-2}$ °C km^{-1}). Thus, only when $grad_{min} < grad_{LIM}$, the frontal zone is identified (see Appendix A).

The SST gradient minimum outside the frontal zone ($grad_{min2}$) is also computed. When $grad_{min2}$ is lower than $grad_{LIM}$, we look for a second frontal zone applying the methodology described in Appendix A to the SST gradient outside the first frontal zone. After this step, $grad$ outside the two frontal zones is always lower than $grad_{LIM}$. Then, the two frontal zones are compared to identify the main upwelling front and the secondary front. To this goal, the temperature differences across the first ($DT1$) and the second ($DT2$) frontal zone are calculated as the SST differences between the extremities of the frontal zones. The mean SST gradient in the first ($grad1$) and the second ($grad2$) frontal zones are also computed. If $\frac{1}{2}\frac{DT2}{DT1}+\frac{1}{2}\frac{grad2}{grad1} \leqslant 1$ ($\frac{1}{2}\frac{DT2}{DT1}+\frac{1}{2}\frac{grad2}{grad1} > 1$), then the first (second) front is considered more intense than the second (first) one. In this case, the first (second) front is the main upwelling front and the second (first, respectively) front is the secondary front. For example, in Figure 1c,d, two fronts are identified around 75 km and 200 km from the coast. The offshore front corresponds to a filament created by a deflection of the coastal jet. Over the nearshore frontal zone, $DT1$ = 2.1 °C and $grad1$ = 0.03 °C km^{-1}, while over the offshore one, $DT2$ = 2.0 °C and $grad2$ = 0.02 °C km^{-1}. The nearshore front being more intense ($\frac{1}{2}\frac{DT2}{DT1}+\frac{1}{2}\frac{grad2}{grad1} = 0.86$), it is identified by the algorithm as the main upwelling front.

Instead of presenting a frontal zone with intense cross-shore SST gradient and low $grad$ outside of it, ∼3% of the analyzed maps present an almost homogeneous $grad$ over the 300 km nearshore. This configuration does not correspond to a well-defined upwelling front separating coastal cold waters from warm offshore waters. Those cases correspond to the detection of a very wide "frontal zone" (⩾ 150 km) and they are discarded from the analysis. For the other maps where a frontal zone is detected, the front is defined on the SST map as the T_0 isotherm, with T_0 being the mean SST over the frontal zone.

2.2.3. Determination of the Front Characteristics

The front parameters are inferred from the smoothed SST profile over the (main) frontal zone. The front width (dl) is computed as the distance between the frontal zone extremities, while the front intensity can be estimated from the SST difference between the frontal zone extremities (DT) and from the cross-front SST gradient ($\frac{DT}{dl}$). The position of the front (DX) is computed as the distance from the coast to the center of the frontal zone.

To study the temporal variability of the front characteristics (Section 3), the upwelling front detection method is applied to the 37°S–36.5°S area over the 2003–2016 upwelling period. First, for each month, we compute the percentage of daily maps where an upwelling front is actually detected ("probability of detecting a front", Section 3.2.1). Second, to study the front intensity, $T_{offshore} - T_{nearshore}$, DT, dl and $\frac{DT}{dl}$ are computed for each daily map over the 2003–2016 upwelling months. Monthly and yearly means, as well as a climatology are then obtained by time-averaging these daily values (Section 3.2.2). Finally, to analyze the impact of the jet meanders on the front position, an histogram of DX is computed for each jet configuration (Section 3.2.3). This histogram is obtained using the front positions detected for all days presenting such jet configuration.

2.3. Statistical Validation of the Detected Fronts

To verify whether isotherm T_0 on the daily map actually separates properly the nearshore cold waters from the offshore region (Section 4.2.1), a statistical test is performed following the methodology described by Cayula and Cornillon [16]. Pixels included in a box, centered on the front mean position and covering the 0.5° latitude range with a zonal width of dx + 50 km, are extracted from the daily map. A SST histogram is computed (Figure 3) and used to define two SST classes (SST colder than T_0 and SST warmer than T_0). To assess whether this segmentation is statistically relevant, θ and the signal-to-noise (σ) ratios defined by Cayula and Cornillon [16] are computed (Table 1). These ratios compare the difference between the mean SST in each class with the standard deviations around these means:

$$\theta = \frac{N_1 N_2}{(N_1+N_2)^2}\frac{(\mu_1-\mu_2)^2}{S_1+S_2} \tag{1}$$

$$\sigma = \left(\frac{(\mu_1-\mu_2)^2}{\frac{N_1}{N_1+N_2}S_1+\frac{N_2}{N_1+N_2}S_2}\right)^{1/2} \tag{2}$$

where N_1 (N_2) is the number of pixels, μ_1 (μ_2) is the mean SST and S_1 (S_2) is the standard deviation in the first (second, respectively) class. The segmentation is considered relevant when $\theta \geqslant 0.7$ and $\sigma \geqslant 4.0$ [16]. To evaluate the robustness of our method for the Chile EBUS, we performed this statistical analysis on a control set of data. Over the 2003–2008 period, from November to March (season with stronger upwelling in the region), 180 daily maps are extracted from six different areas off Central Chile (38°S–37.5°S, 37.5°S–37°S, 37°S–36.5°S, 36.5°S–36°S, 36°S–35.5°S, and 35.5°S–35°S) and analyzed. The results are presented in Section 3.1.1.

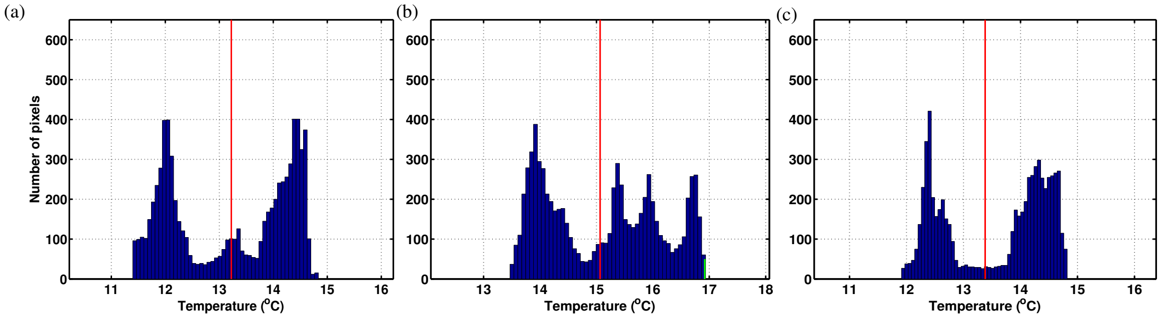

Figure 3. SST histograms of the region within 50 km from the front detected by the algorithm for: (**a**) 13 December 2010; (**b**) 23 March 2007; and (**c**) 14 November 2016. Red line represents T_0.

Table 1. θ and σ ratios computed for several daily SST maps (area within 50 km from the detected upwelling front) and using T_0 as the threshold temperature.

	θ	σ
10 January 2004	0.9	5.1
19 May 2004	0.8	4.4
02 March 2005	0.9	5.1
10 March 2005	0.9	5.1
05 April 2005	0.8	4.6
11 January 2005	0.8	4.8
15 January 2007	0.7	3.5
23 March 2007	0.8	4.0
10 March 2009	0.9	5.8
13 December 2010	0.9	5.0
14 November 2016	0.9	6.1

3. Results

3.1. Atmospheric and Oceanic Forcing

Here, we first describe the oceanic and atmospheric conditions over the studied area that could potentially affect the upwelling front.

3.1.1. Local Atmospheric Forcing and Its Impact on the SST

The front characteristics depend on the SST field within 300 km from the coast that is primarily forced by the solar heat flux and the wind stress [24]. Figure 4 shows the temporal variability of the SST conditions during the first and last two years of the study period. Variations in the area are dominated by the seasonal cycle. The short-wave flux climatology presents a maximum in January and a minimum in June while the alongshore coastal wind is upwelling-favorable from September to April, with stronger intensity (>0.08 N m^{-2}) from November to March and a maximum in January (Figure 5a). Offshore, the SST is little affected by coastal upwelling and the seasonal cycle of $T_{offshore}$ is strongly linearly correlated (R = 0.98) to solar heating with a 1.5 month lag (Figure 5b). The seasonal cycle of $T_{nearshore}$ is also correlated (R = 0.98) to the solar heating with the same lag, but its amplitude is reduced by 40% compared to $T_{offshore}$ because upwelling is slowing heating down when the solar flux is the strongest. The effect of upwelling can be evidenced from the seasonal cycle of $T_{offshore} - T_{nearshore}$ that is maximum in March and minimum in September. This seasonal cycle is correlated to the alongshore wind stress seasonal cycle with a lag of two months (R = 0.97). Thus, although wind conditions are upwelling-favorable during September–April, the imprint of this forcing on the SST is from November to June. This is why we now refer to the November–June period as the "upwelling months". Note that this delay has already been evidenced and explained by [13] (see Section 1).

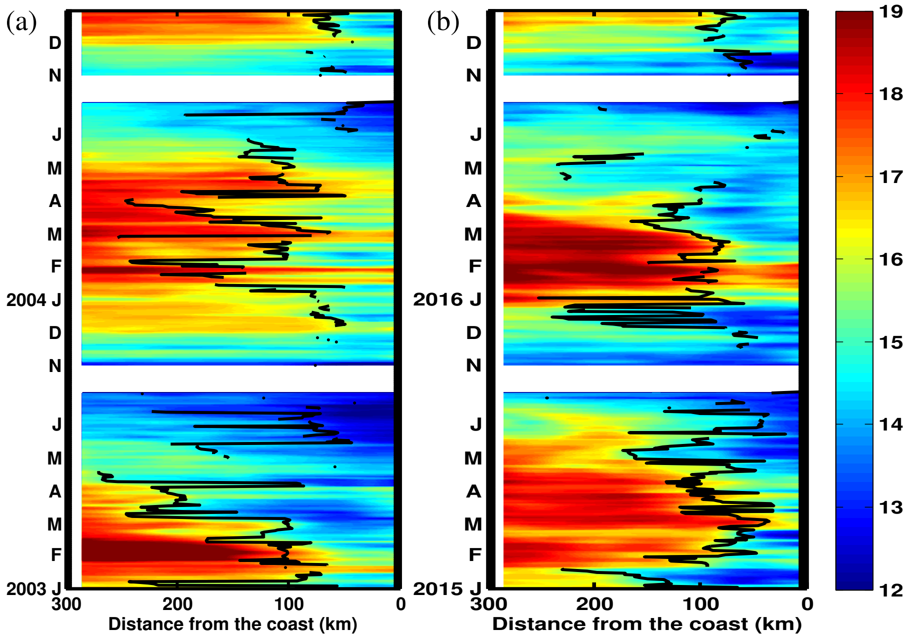

Figure 4. Mean daily SST (in °C) between 37°S and 36.5°S with respect to the distance from the coast and time during the upwelling months (November–June) for years: (**a**) 2003–2004; and (**b**) 2015–2016. Black line marks the center of the stronger gradient zone ("upwelling front") identified by the algorithm.

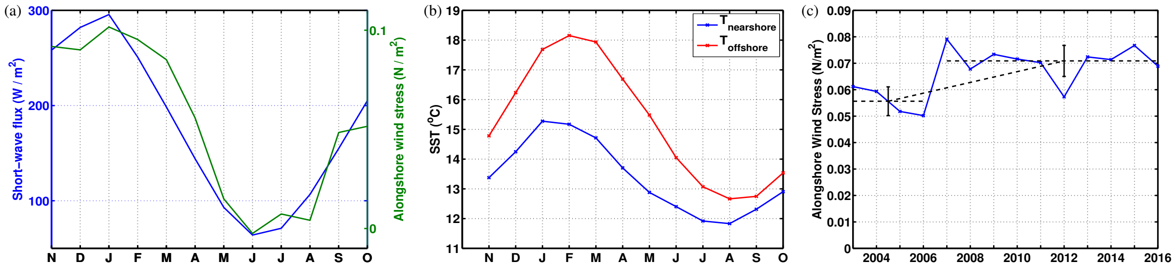

Figure 5. (**a**) Seasonal cycle of the short-wave downward heat flux (blue line, in W m^{-2}) and the alongshore coastal wind stress intensity (green line, in N m^{-2}). (**b**) Seasonal cycle of the mean SST (in °C) at 1 km from the coast (blue line) and at 300 km from the coast (red line). (**c**) Yearly means of the alongshore coastal wind stress intensity (in N m^{-2}). Black lines represent the averages (horizontal lines) and standard deviations (vertical lines) over the 2003–2006 and the 2007–2016 periods.

When removing the climatology, the daily nearshore SST anomalies are negatively correlated (R = −0.42) during the upwelling month to the alongshore wind stress intensity averaged over the previous 10 days. This underlines the importance of wind stress forcing on $T_{nearshore}$ for shorter timescales than the seasonal one.

Monthly values of $T_{nearshore}$ anomalies are only weakly correlated to the Oceanic Niño Index (ONI), [42]. Indeed, the highest correlations are obtained with a three-month delay and do not exceed 0.24. For example, differences in nearshore SST anomalies between January–June 2003 and November 2003–June 2004 (Figure 4) cannot be explained by the ENSO cycle. Indeed, both periods correspond to neutral ENSO conditions (not shown) while monthly anomalies of $T_{nearshore}$ are weak ($\leqslant$0.5 °C) during the first period and warm during the second one (⩾0.5 °C during Spring and even ⩾1°C during Fall 2004). The ENSO influence is more notable during 2014 and 2015, when the ONI shows warm (ONI ⩾ 0.5 °C) and increasing ENSO conditions from November 2014 (not shown). Consistently with the three-month delay between the ONI and $T_{nearshore}$ anomalies, the latter increases from February 2015. The ONI values ⩾ 1.5 °C from August 2015 to March 2016 (not shown) indicates a very strong ENSO phase that would affect $T_{nearshore}$ from November to June. $T_{nearshore}$ anomalies are indeed warm and ⩾0.5 °C, except in December, February and March ($|T_{nearshore}| \leqslant 0.5$ °C, neutral conditions).

The yearly values of $T_{nearshore}$ are correlated to those of $T_{offshore}$ (R = 0.83) but the correlations with the local forcing (both the alongshore wind and the solar heating) are not significant (p-value > 0.05). This suggests that the interannual variations of $T_{nearshore}$ and of $T_{offshore}$ are dominated by large-scale variations instead of local atmospheric conditions. However, neither the yearly values of $T_{nearshore}$ nor those of $T_{offshore}$ are significantly correlated to the ONI (not shown).

Although correlations between the yearly values of $T_{offshore} - T_{nearshore}$ and of the alongshore wind intensity are not significant, on a longer time scale, the trend of the wind conditions and the cross-shore SST difference are consistent. Indeed, in the studied area, the alongshore wind stress intensity presents an intensification after 2007 (Figure 5c), as described by [43], and explained by a poleward displacement of the South East Pacific anticyclone. The alongshore wind stress intensity averaged over the 2007–2016 period is 25% stronger than over the years 2003–2006 while $T_{offshore} - T_{nearshore}$ is enhanced by 24% (Section 3.2.2). This 0.5 °C increase of $T_{offshore} - T_{nearshore}$ is mainly due to a 0.6 °C cooling of $T_{nearshore}$ ($T_{offshore}$ remaining almost unchanged, not shown) due to the coastal upwelling intensification.

3.1.2. Coastal Jet Circulation

It has been suggested that the position of the SST upwelling front is related to the position of the coastal jet [7]. Here, the coastal circulation is studied using surface geostrophic currents (see Section 2.1) to identify the most frequent coastal jet configurations. First, the number of coastal jets present within 300 km from the coast are computed. No jets are detected for 21% of the daily maps, only one jets is detected for 64% of cases, and 15% of maps present two jets. From all maps where only one jet is detected, a distance from the coast Probability Density Function (PDF) is computed using all pixels included in the jet (Figure 6a). The PDF presents two maxima at ∼25–75 and 200–225 km from the coast, separated by a minimum at ∼100 km. This shows that two positions for the jet are most probable (within 100 km from the coast, centered ∼50 km, or offshore from 100 km from the coast, centered ∼225 km). For all maps where two jets are detected, pixels with alongshore velocities above 0.1 m s^{-1} are classified whether they belong to the most nearshore or the most offshore jet. A first distance from the coast PDF is computed using all pixels located in the most nearshore jets, and a second one is computed using all pixels located in the most offshore jets (Figure 6b). These PDFs show that, when two jets are detected, the most nearshore is preferentially located at ∼50 km from the coast and the most offshore is at ∼250 km. Almost all most nearshore (offshore) jets are located within (offshore from, respectively) ∼150 km from the coast. We now call "nearshore jet" ("offshore jet") a jet with a center within (offshore from, respectively) 125 km from the coast. The distance from the coast to the jet center is defined as the mean distance from the coast of all pixels included in the jet. Climatologies of the numbers of maps with no jet, with one nearshore jet, with one offshore jet, and with two jets ("jet configurations") are computed for the upwelling months (Figure 6c). Maps with no jet are more frequent during spring (November–December) and late fall (June), when they represent ∼30% of the daily maps. From January to May, maps without any jet only represent ∼10–20% of cases. The presence of only one nearshore jet represents ∼55% of the maps during November. This proportion decreases during the upwelling months down to 4% in June. On the contrary, the presence of only one offshore jet is rare (10% of the cases) during November and then increases during the next months up to ∼70% of maps in April. Finally, two jets are detected for ∼20% of cases from January to April (with a maximum of ∼30% in May) and for ∼5–10% of cases during spring and late Fall.

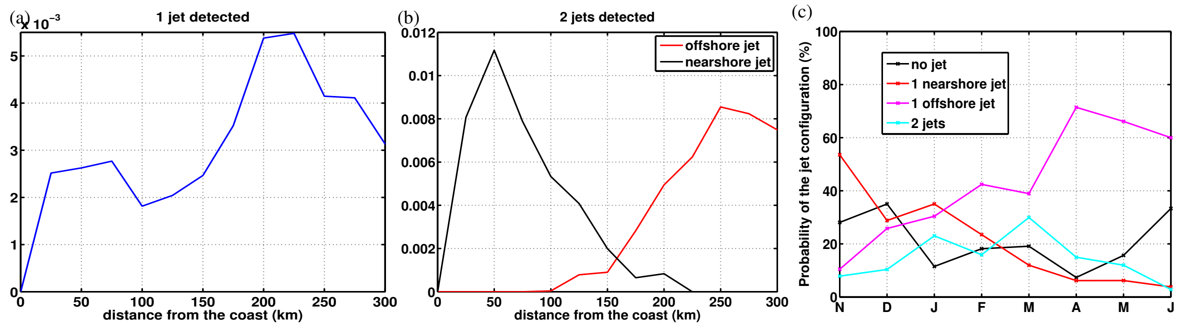

Figure 6. (**a**,**b**) Distance from the coast Probability Density Functions (PDF) of pixels with alongshore surface currents above 0.1 m·s^{-1} in the 300 km nearshore. PDFs are computed using the 2003–2016 geostrophic currents daily maps during upwelling months with: (**a**) only one jet in the 300 km nearshore; and (**b**) two jets in the 300 km nearshore. Black (red) line represents the PDF for pixels associated with the nearshore (offshore, respectively) jet. (**c**) Numbers of daily maps (in %) with no jet in the 300 km nearshore (black line), with only one jet in the 300 km nearshore, located within (red line) and offshore from (magenta line) the 125 km nearshore, and with two jets in the 300 km nearshore (cyan line). Numbers of maps where normalized by the number of analyzed maps during the selected month.

3.2. The Front Characteristics Variability

3.2.1. Probability of Detecting a Front

The percentage of daily maps where an upwelling front is actually detected is above 50% from November to June (Figure 7a), period that corresponds to the "upwelling months" (Section 3.1.1). This is why the front characteristics presented in this paper are computed only during those months. The number of daily maps with an upwelling front is maximum in March, where almost 100% of the maps exhibit an upwelling front. This is consistent with the alongshore wind stress maximum in January and the two-month lag between the wind forcing and its impact on the SST field (Section 3.1.1).

The yearly values of the number of days with an upwelling front evidence an increase after 2007 (Figure 7b) and the mean value over the 2007–2016 period is 14% stronger than over the 2003–2006 period. This is consistent with the increase in upwelling-favorable wind conditions over the same period (Section 3.1.1). However, the standard deviations around these means are large and a longer time series is necessary to confirm this tendency.

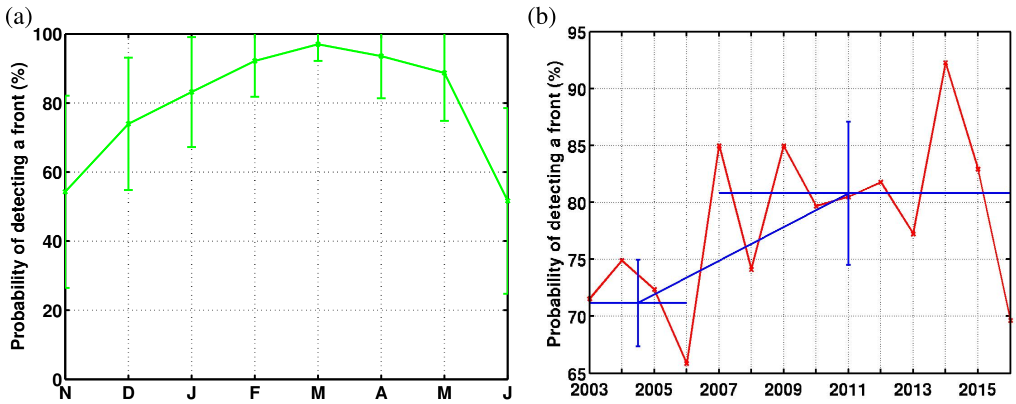

Figure 7. Number of daily SST maps presenting an upwelling front compared to the total number of maps (in %): (**a**) seasonal cycle (climatology over the 2003–2016 period, error bars represent the standard deviations); and (**b**) yearly values (red line). Blue lines represent the averages (horizontal lines) and standard deviations (vertical lines) over the 2003–2006 and the 2007–2016 periods.

3.2.2. Front Intensity

Monthly values of the front intensity show that DT is highly correlated with $T_{offshore} - T_{nearshore}$ (Table 2), suggesting a driving of DT by $T_{offshore} - T_{nearshore}$. Not surprisingly, dl is strongly correlated to DT and so is $\frac{DT}{dl}$. These results evidence that a stronger (weaker) $T_{offshore} - T_{nearshore}$ is associated with enhanced (reduced) DT, a wider (narrower) front and also a stronger (weaker, respectively) $\frac{DT}{dl}$.

Table 2. Correlations between the time-averaged (monthly mean, yearly mean and seasonal cycle) front characteristics, computed from the daily maps.

	R($\boldsymbol{DT}$,$\boldsymbol{T_{offshore} - T_{nearshore}}$)	R($\boldsymbol{DT}$,$\boldsymbol{dl}$)	R($\boldsymbol{DT}$,$\boldsymbol{\frac{DT}{dl}}$)
monthly mean	0.86	0.78	0.77
yearly mean	0.88	0.89	0.64
climatological seasonal cycle	0.93	0.93	0.97

The seasonal cycles of DT, $\frac{DT}{dl}$, and dl show a maximum during February and March (Figure 8). Indeed, DT is increased by 81% in March compared to November. This is consistent with the $T_{offshore} - T_{nearshore}$ intensification during summer (Figure 8a) that results from the SST response to the increased upwelling-favorable wind conditions (Section 3.1.1). Note, however, that the increase in $T_{offshore} - T_{nearshore}$ between March and November (128%) is stronger than the increase in DT. This is likely due to the seasonal cycle of SST gradients associated with mesoscale activity. Indeed, mesoscale structures can create cross-shore SST gradients out of the main upwelling front e.g., (Figure 1b). In those cases, $T_{offshore} - T_{nearshore}$ can be approximated by the sum of DT and the SST differences across all these secondary fronts. The occurrence of such secondary SST gradients is enhanced during summer [34], increasing the difference between DT and $T_{offshore} - T_{nearshore}$. Between March and November, the front is also broadened (Figure 8b). However, the increase in dl (40%) is reduced compared to DT, so that the mean cross-shore gradient across the front $\frac{DT}{dl}$ is also slightly enhanced (31%, Figure 8c).

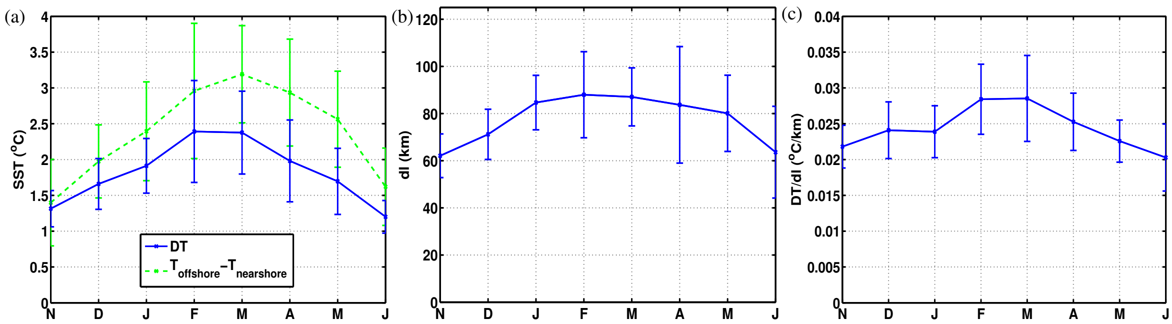

Figure 8. Climatology of mean front characteristics using daily SST maps during the 2003–2016 upwelling months: (**a**) SST difference (in °C) across the front (DT, plain blue line) and SST difference between the coast and 300 km offshore ($T_{offshore} - T_{nearshore}$, dotted green line); (**b**) front width (dl, in km); and (**c**) cross-front SST gradient ($\frac{DT}{dl}$, °C km^{-1}). Error bars represent the standard deviations.

Yearly values show the increase of $T_{offshore} - T_{nearshore}$ discussed in Section 3.1.1 (Figure 9a). Resulting from the stronger $T_{offshore} - T_{nearshore}$, DT is also enhanced by 17% during 2007–2016 compared to the 2003–2006 period (Figure 9b). A slight increase (12%) in the front width can also be observed (Figure 9c), although the high interannual variability makes it hardly distinguishable. As a result, $\frac{DT}{dl}$ is almost unchanged and a longer time series would be necessary to identify any increase.

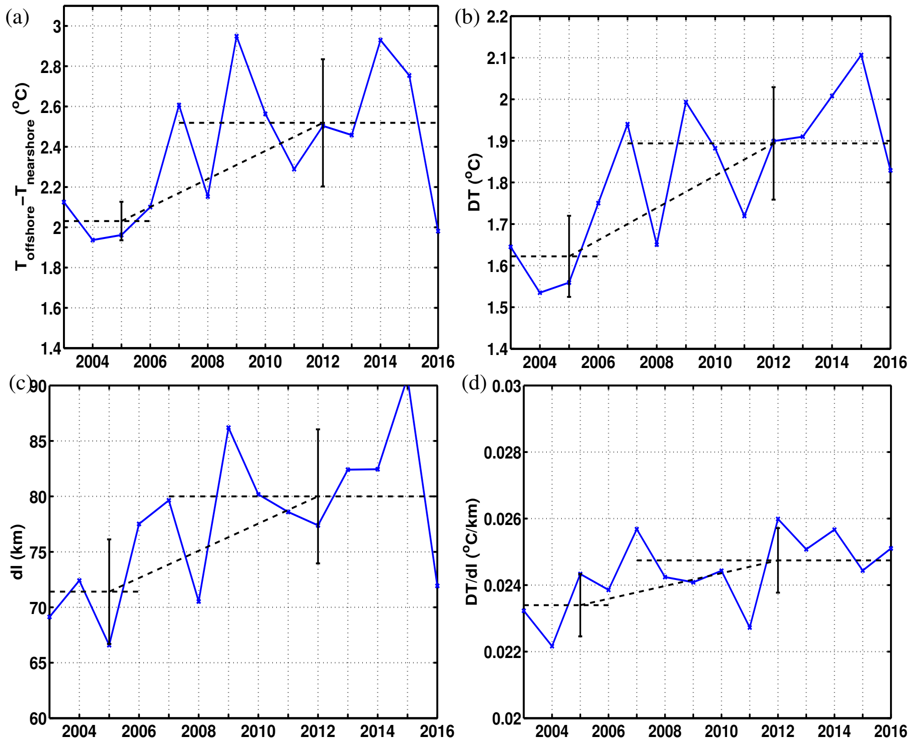

Figure 9. Mean front characteristics (yearly averages for the fronts detected on daily SST maps, blue line). Black lines represent the averages (horizontal lines) and standard deviations (vertical lines) over the 2003–2006 and the 2007–2016 periods: (**a**) SST difference (in °C) between the coast and 300 km offshore; (**b**) SST difference (in °C) across the front; (**c**) Front width (in km); and (**d**) cross-front SST gradient (in °C km^{-1}).

3.2.3. Front Position

The position of the front (DX) presents high temporal variability, and can vary from 100 km to 200 km from the coast within a few days (Figure 4). The standard deviations around the yearly values are large (∼100–150 km) and data do not show any trend over the 2003–2016 period (Figure 10). There was no direct relation between the front position and the coastal wind or heat fluxes (the correlation between the two time series are not significant).

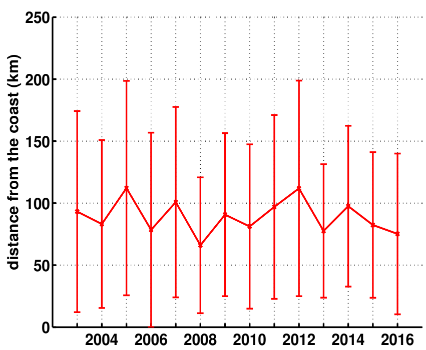

Figure 10. Seasonal cycle of the distance between the coast and the upwelling front (in km). Error bars represent the standard deviations.

We now study the relation between the coastal jet configuration and the front position. Figure 11a shows that the presence of only one nearshore jet is associated with a front located very nearshore, between 50 and 100 km from the coast for ∼80% of the cases. In this jet configuration, $DX > 125$ km represents ∼10% of the cases. When two jets are detected, the front is also preferentially located between 50 and 100 km from the coast (∼65% of the cases), but more offshore fronts (>125 km) are more frequent (∼30%) than when only one nearshore jet is detected. When no jet are detected, the front position is located from 50 to 125 km offshore for 80% of days. Finally, when only one offshore jet is identified, the front position is much less restrained nearshore, and the proportion of fronts is ∼10% for all positions between 50 and 250 km (with a maximum of 15% at 50 km from the coast). During the "upwelling months", the probability of detecting only one nearshore jet (that is associated with more nearshore fronts) decreases and the probability of detecting one offshore jet (associated with more offshore fronts) increases (Figure 6c). This explains the fact that the mean distance from the coast to the front (and the standard deviation) increases during the "upwelling months", from 80 km in November to 150 km in May (Figure 11b).

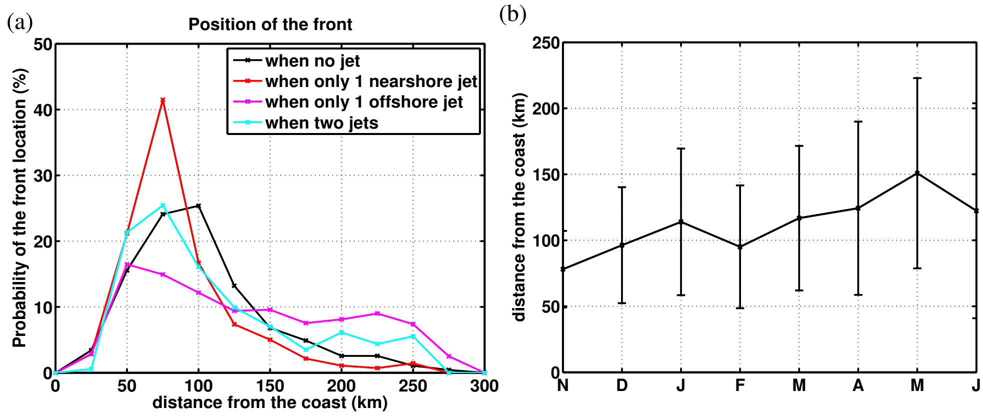

Figure 11. (**a**) Histograms of DX computed using all daily maps with the same jet configuration. DX is normalized by the total number of maps with the considered jet configuration. Black line corresponds to the maps with no jet in the 300 km nearshore. Red (magenta) line corresponds to the maps with only one jet in the 300 km nearshore, located within (offshore from, respectively) 125 km from the coast. Cyan line corresponds to the maps with two jets in the 300 km nearshore. (**b**) Seasonal cycle of the mean front position. Error bars represent the standard deviations.

4. Discussion

4.1. Strength and Limitations of the Front Detection Method

4.1.1. Strength

In EBUS, a multiplicity of intense SST gradients are present near the frontal zone. This make difficult the upwelling front identification among all the secondary fronts. Our method is able to detect this main front, despite the large diversity of situations that can be observed. For example, in Figure 12a,c, the geostrophic circulations are very similar, with a large anticyclone centered on 36.3°S, 77.3°W in both cases. Nevertheless, the SST fields are different. Indeed, in Figure 12a,b, the coastal upwelled waters advected by the eddy result in a relatively homogeneous (cold) SST from the coast to the western eddy side, and the upwelling front is located offshore from the anticyclone. In Figure 12c, although cold waters are also advected by the eddy, SST on the eastern eddy side is still warmer than closer to the coast. As a result, two fronts are detected by the algorithm on each eddy side. The nearshore front, which is more intense, is the main upwelling front (Figure 12d). On 11 January 2005, a cyclone advects coastal waters offshore, creating a cold filament (Figure 12e). Although the SST inside and outside the filament differs by ∼1 °C, the reduced size of this feature leads to a very weak imprint on the mean SST (Figure 12f) and no secondary front is detected by our method. On 10 March 2009, the mean SST (Figure 12g) shows the presence of two strong SST gradients ∼50 km and 150 km from the coast. The offshore frontal zone presents a stronger SST difference and a stronger mean SST gradient (Figure 12h). Thus, our method considers that the coastal SST water extends from the coast to the offshore front, which is identified as the main upwelling front. In some cases, a mesoscale structure can deform the upwelling front, so that the front in this area is no longer oriented in the alongshore direction and can even be locally cross-shore oriented (Figure 12i). Our method is able to capture such features and to define a statistically consistent front (Figure 12i,j and Table 1). This is because the front is defined as an isotherm (thus, there is no condition over the front direction) and because, even in such cases, there are two very low cross-shore gradient zones, nearshore from the filament base (in the cold tongue), and offshore from the filament extension. Thus, the algorithm is able to compute the mean SST between these two zones and to define the front.

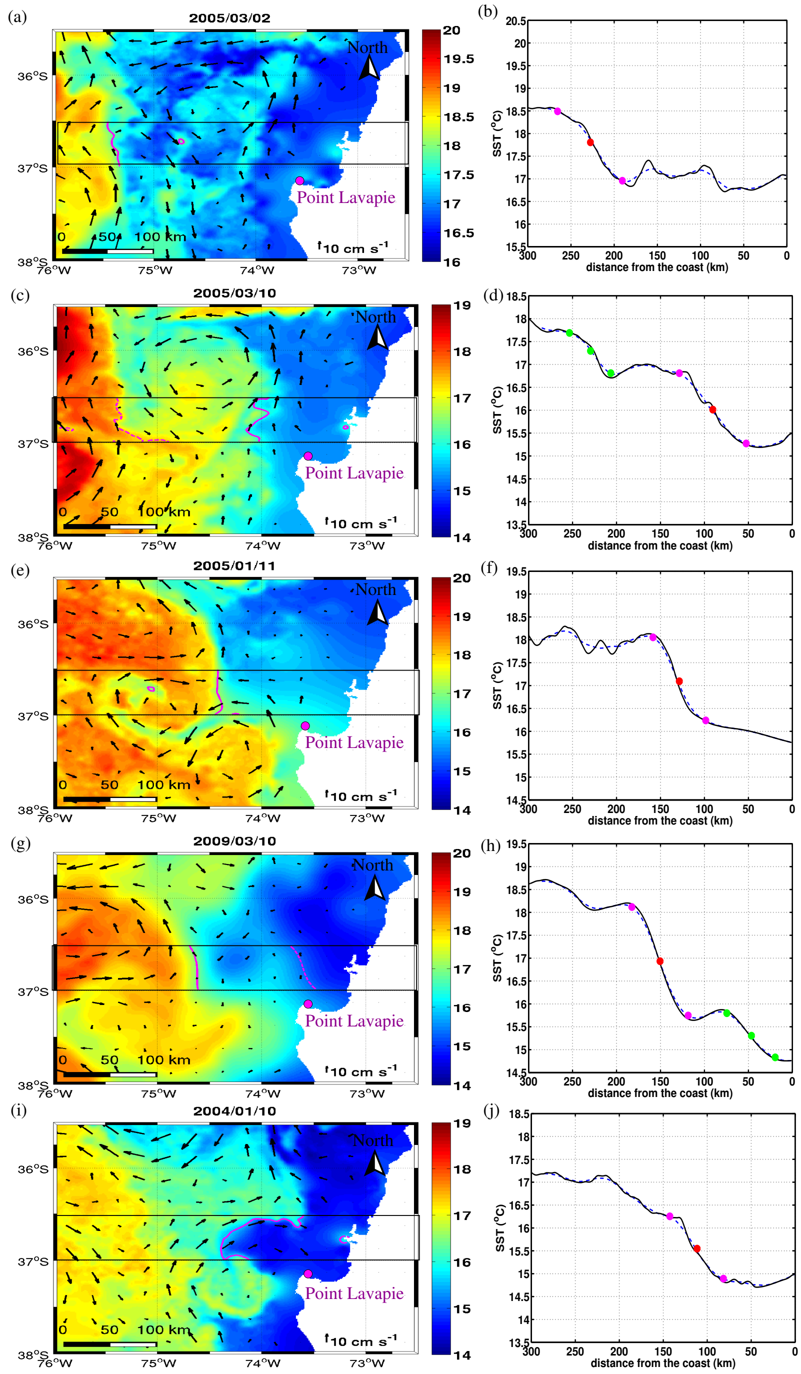

Figure 12. Same as Figure 1 for: 2 March 2005 (**a**,**b**); 10 March 2005 (**c**,**d**); 11 January 2005 (**e**,**f**); 10 March 2009 (**g**,**h**); and 10 January 2004 (**i**,**j**).

The algorithm has proved to be robust off Central Chile, where it was able to distinguish the main upwelling front from this strong mesoscale field. Mesoscale SST gradients in this region are particularly strong [34]. Thus, the method can all the more be applied to SST fields presenting less strong SST mesoscale field such as other areas, time-averaged SST maps, or lower resolution products. In addition, our method analyzes the SST daily conditions to compute case-by-case the most adequate isotherm T_0 that defines the front. This is why this methodology can be applied to different time-periods and other EBUS regions without major code modifications.

4.1.2. Limitations

Nevertheless, our method includes some arbitrary parameters (e.g., $grad_{LIM}$) that were empirically defined by applying the algorithm to HCS areas included between 38°S and 35°S. These parameters may need to be adjusted for other areas and make the method somewhat subjective. For this reason, we included in the algorithm a step that analyzes the frontal zone interval identified to verify afterward whether the interval extremities actually correspond to edges in the cross-shore SST gradient (see Appendix A).

The method described here only detects the main upwelling front in a 0.5° latitude range. This latitude range was also empirically determined. Indeed, the meridional extension of the studied region must be large enough to filter noise when computing the mean SST with respect to the distance from the coast. However, this extension must also be reduced enough so that one isotherm can actually define the front on the daily SST map (this isotherm must be located in the strong cross-shore gradient area for all latitudes in the studied region), and 0.5° was the largest meridional extension that fulfill this requirement. To obtain a front defined over a larger region, the following method could be applied: for each latitude lat_1, the algorithm is applied to the area between $lat_1 - 0.25°$ and $lat_1 + 0.25°$ and the value of the front temperature $T_0(lat_1)$ is computed. The upwelling front is then defined on the SST map for each latitude lat_1 as the point where $SST = T_0(lat_1)$.

When clouds are present over a pixel, the high resolution infrared measurement are unavailable and the available micro-wave satellite measurements present lower resolution (25 km). This could affect the front detection and the measures of dl and $\frac{DT}{dl}$. However, considering its typical size (∼50–100 km, Figure 8b), the upwelling frontal zone is large enough to be well defined even on 25 km-resolution observations. In addition, Morales et al. [44] found that missing data in the case of satellite surface Chl-a off central-southern Chile, which can be mostly attributed to cloud coverage, represent 55–60% of the data, with seasonality not influencing these results. Thus, we assume that the impact of clouds on the front characteristics and their seasonality is weak.

4.2. Comparison of the Front Detection Method with Previous Works

4.2.1. Consistency with the Front Definition by Cayula and Cornillon (1992)

The front detection method from Cayula and Cornillon [16] was designed to detect all fronts present in a given area and not just the main upwelling front. However, it provides a method to assess whether a given isotherm on a SST map separates two water regions with statistically different SST characteristics. To evaluate whether the isotherm T_0 (used in our method to define the upwelling front) do represent a threshold separating the coastal cold water from offshore, this statistical test is applied to the fronts detected over 180 maps (Section 2.3). In 55 maps, no front is detected (31% of the total). A frontal zone larger than 150 km is detected in five maps (3% of the total), and, thus, discarded from the test. Over the 120 remaining maps where a relevant front has been detected, 19 maps (15% of 120) do not pass the test (because $\theta < 0.7$ or because the signal-to-noise ratio is <4.0). However, among these 19 cases, 12 of them correspond to a front with a nearshore extremity closer than 25 km from the coast. In those cases (e.g., Figure 13 and Table 1), there are too few pixels between the front and the coast to form a population statistically comparable to the class of pixels warmer than T_0. The seven other maps (6% of the 120 maps) correspond to cases where the algorithm fails to properly identify an upwelling front.

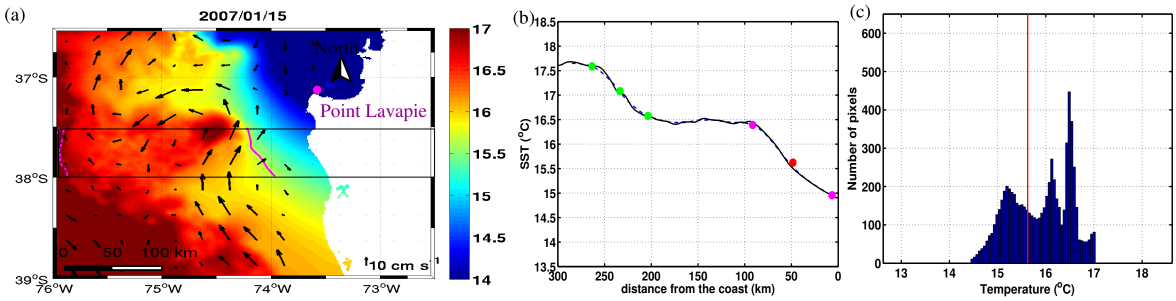

Figure 13. (**a**,**b**) Same as Figure 1a,b; and (**c**) same as Figure 3, for 15 January 2007 and the 38°S–37.5°S zone as studied area.

4.2.2. Consistency with In Situ Measurement

The front position computed with the new method is now compared to the front identified using in situ observations (Figure 14). During the PHYTO-FRONT cruise, in both cross-shore transects, ship measurement evidenced a narrow zone of strong surface temperature and salinity gradients between two consecutive stations [14]. These zones correspond to SST values ∼17 °C for both transects and were identified as the upwelling front. Although in situ measurements at 3.5 m depth and satellite SST observations differ by up to 1 °C in the offshore region, the front automatically detected by our method is located between the two stations delimiting the front extension in Morales et al. [14].

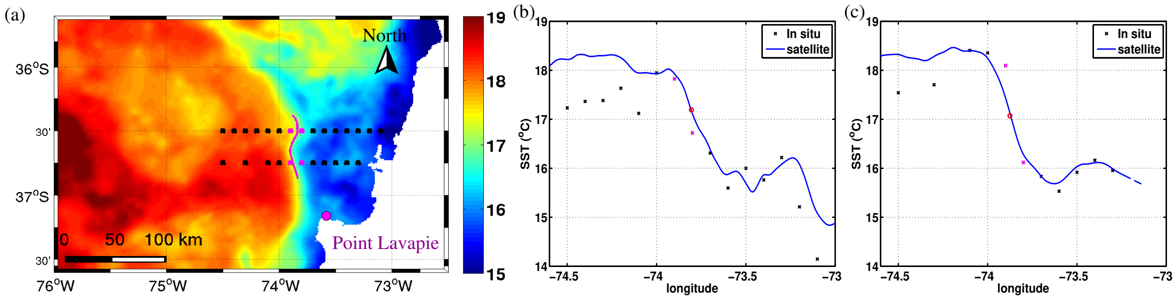

Figure 14. (**a**) Mean satellite SST (colors, in °C) during 4–6 February 2014. Black and magenta crosses mark the PHYTO-FRONT sampling stations positions. Magenta line represents the front detected on the mean SST map for the 36.875°S–36.375°S zone. (**b**) Mean satellite SST at 36.5°S during 5–6 February 2014 period (blue line). Black and magenta crosses indicate the 3.5 m depth in situ temperature along the 36.5°S transect. Red dot marks the value of T_0 computed using the 05–06 February 2014 SST included in the 0.5° latitude-large zone around 36.5°S. (**c**) Same as (**b**) but for latitude 36.75°S and 5–6 February2014 period. Magenta crosses in (**a**–**c**) indicate the stations delimiting the front according to Morales et al. [14].

4.3. Front Characteristics Variability off Central Chile

4.3.1. Errors and Uncertainties

The front characteristics show high variability at all temporal scales and the standard deviations around the climatological and yearly values presented here are large. As a result, the relatively small variations in the seasonal cycle (Figure 8c) and in the trend (Figure 9d) during 2003–2016 for $\frac{DT}{dl}$ are located within the standard deviation, and, thus, are not statistically significant. In the next years, the inclusion of new yearly values may reduce the uncertainty in the evolution of $\frac{DT}{dl}$ so that a significant trend may be identified out of a longer timeseries. The front position DX also shows large standard deviations and no trend can be identified (Figure 10). On the contrary, the variations in the seasonal cycles and the trends of the probability of detecting a front (Figure 7), DT (Figures 8a and 9b) and dl (Figures 8b and 9c) are significant.

4.3.2. Jet Configuration and Front Position

A striking result of this article is the statistical analysis of the coastal jet position and its relation with the position of the upwelling front. Four most common configurations have been identified (no jet, one nearshore jet, one offshore jet, and two jets), which is consistent with the configurations observed in the studied cases from previous studies [7,32,33]. Our study shows that the most common configuration is the presence of one offshore jet. We also evidence a seasonal variability of the proportion of each configuration, consistent with the seasonal current maps from Aguirre et al. [31], that shows a nearshore jet in spring, two jets during summer, and an offshore jet in fall. This westward propagation of the coastal jet north of Point Lavapie during summer has been related to the negative wind stress curl conditions [31]. Coastal Ekman pumping facilitates the jet separation from the coast near a cape (the separation occurs earlier and the jet propagates farther) [45]. The offshore jet propagation during the upwelling season is also a known feature in the California EBUS, where the importance of wind stress curl [46,47], interaction with alongshore topography [48] and beta-effect (Rossby wave dynamics) [5,46] have been underlined. The main upwelling front is commonly described as co-located with the coastal jet (e.g., [7]). We show here that this is true when the jet is nearshore, nevertheless the presence of only one jet located offshore is associated with very different front positions. Nearshore jets (and, thus, colocated fronts) are more frequent during spring/early summer. At the beginning of the upwelling season, the coastal jet formation has been directly linked to the upwelling-induced cross-shore density gradient [45,47–49]. The coastal jet is created by geostrophic adjustment to the SST front, and thus is co-located with it. Offshore jets are more frequent at the end of the upwelling period, and the jet meanders are no longer related to the local SST gradient.

4.3.3. Reinforcement of the Upwelling Front in EBUS

Our study shows a reinforcement of the upwelling front (more frequent front, with a more intense cross-front SST difference) linked to the intensification of alongshore coastal winds at 37°S after 2007. However, this results may not be extrapolated to other regions of the HCS or other EBUS. Indeed, the wind intensification has been linked to a poleward displacement of the South East Pacific anticyclone. This displacement favors upwelling conditions off Central Chile but may decrease the coastal wind in the northern part of the HCS [50], and the future of coastal winds in the HCS under climate change conditions remains an open question [50–53].

5. Conclusions

An algorithm to identify the main upwelling front from high resolution SST daily maps is used here to automatically compute the front magnitude, width and position. The main asset of this method is its ability to automatically identify the main front among all strong SST gradients created by mesoscale and submesoscale features. In addition, although some arbitrary parameters may need to be adjusted, the method is general enough to be applied to different Eastern Boundary Upwelling Systems. However, clouds making unavailable infrared high resolution measurements, the cloud coverage may affect the results, in particular when studying very narrow (<25 km) upwelling fronts.

This algorithm has been applied to an area in the highly productive region off Central Chile (37°S–36.5°S) during 2003–2016 to analyze the front characteristics and their temporal variability. We show that the intensity of upwelling-favorable wind conditions is the main driver of the probability of detecting a front, and also of the front magnitude and its width, for both the seasonal cycle and the long-term trend. The coastal wind intensification after 2007 (+25%) is responsible for an increase in the percentage of days presenting a main upwelling front (probability of detecting a front increased by 14%), in the SST difference across the front (by 17%) and in the front width (by 12%), while changes in the cross-front SST gradient are very low. On the contrary, the position of the front is highly variable within a few days and does not show any trend over the studied period. In addition, this position is not related to the wind conditions but to the coastal jet meanders. The coastal jet(s) location(s) during the upwelling months has (have) been detected to obtain for the first time a statistics over the years 2003–2016 and to identify the most frequent configurations. We show that the presence of a very nearshore jet (∼25–75 km from the coast) is associated with a front located very close while when the coastal jet meander is located offshore from 125 km from the coast, the front is not co-located with the jet.

Similar front analysis could be performed for other Eastern Boundary Upwelling System areas to monitor the long-term variability associated with climate change and to identify similarities and differences in their evolution. The analysis of other oceanic fields (from satellite or in situ observations) in the Coastal Transition Zone can now be related to the front characteristics defined here. This would be useful to study the impact of the upwelling front fine-scale variations on the biological components and activity.

Author Contributions: V.O., C.E.M., J.B., S.H. and O.P. conceived and designed the experiments; V.O. performed the experiments; V.O. and C.E.M. analyzed the data; J.B., S.H and O.P contributed to the analysis tools; and V.O., C.E.M., J.B., S.H. and O.P. wrote the paper.

Acknowledgments: This study was supported by FONDECYT Project 1151299 (C.E.M. and S.H.), FONDECYT 1171895 (S.H. and J.B.), and IMO-Chile funding. The Group for High Resolution Sea Surface Temperature (GHRSST) Multi-scale Ultra-high Resolution (MUR) SST data were obtained from the NASA EOSDIS Physical Oceanography Distributed Active Archive Center (PO.DAAC) at the Jet Propulsion Laboratory, Pasadena, CA, USA (http://dx.doi.org/10.5067/GHGMR-4FJ04). The altimeter products were produced by Ssalto/Duacs and freely distributed by CMEMS (www.http://marine.copernicus.eu/). Wind stress conditions were obtained from the IFREMER at ftp://ig1fdaf:H6RI7tOe@eftp.ifremer.fr/IFREMER_LOPS_blended_wind/longterm_analysis/. Short-wave heat fluxes were produced by the NOCS and obtained at https://rda.ucar.edu/datasets/ds260.3/.

Conflicts of Interest: The authors declare no conflict of interest. The founding sponsors had no role in the design of the study; in the collection, analyses, or interpretation of data; in the writing of the manuscript, and in the decision to publish the results.

Abbreviations

The following abbreviations are used in this manuscript:

EBUS	Eastern Boundary Upwelling System
CTZ	Coastal Transition Zone
SST	Sea Surface Temperature
HCS	Humboldt Current System
ENSO	El Niño Southern Oscillation
SSH	Sea Surface Height
PDF	Probability Density Function
MUR	Multi-scale Ultra-high Resolution
NOCS	National Oceanography Center Southampton
ONI	Oceanic Niño Index

Appendix A. Strong Cross-Shore Gradient Zone “Frontal Zone”) Identification

We describe here the method to identify the frontal zone from the smoothed SST profile (see Section 2.2). The difficulty here is that the intensity of $grad$ is highly variable according to the daily maps, so that a fixed threshold for $grad$ cannot be defined and used to determine the interval extension. The method developed to solve this issue is summarized in Figure A1.

First, we analyze the surroundings of the point x_{min} where $grad = grad_{min}$ to determine the continuous interval where $grad > r \cdot grad_{LIM}$ with r initialized to $\frac{1}{2}$. The width interval dx is computed. When dx is larger than 50 km and the mean SST gradient over the interval is lower than $grad_{LIM}$, the interval is considered to be the frontal zone. It is also the case when $dx < 50$ km and the SST difference between its extremities x_1 and x_2 is larger than 0.7 °C. On the contrary, if the interval is narrow ($dx < 50$ km) and with a weak SST difference ($SST(x_1) - SST(x_2) < 0.7$ °C), this interval is considered irrelevant and we newly seek for the frontal zone outside this interval. Finally, if the interval is wide ($dx \geqslant 50$ km) but the mean SST gradient over the interval is larger than $grad_{LIM}$, we restrain the interval around x_{min}: the value of r is increased by 0.1 and we determine the new interval where $grad > r \cdot grad_{LIM}$.

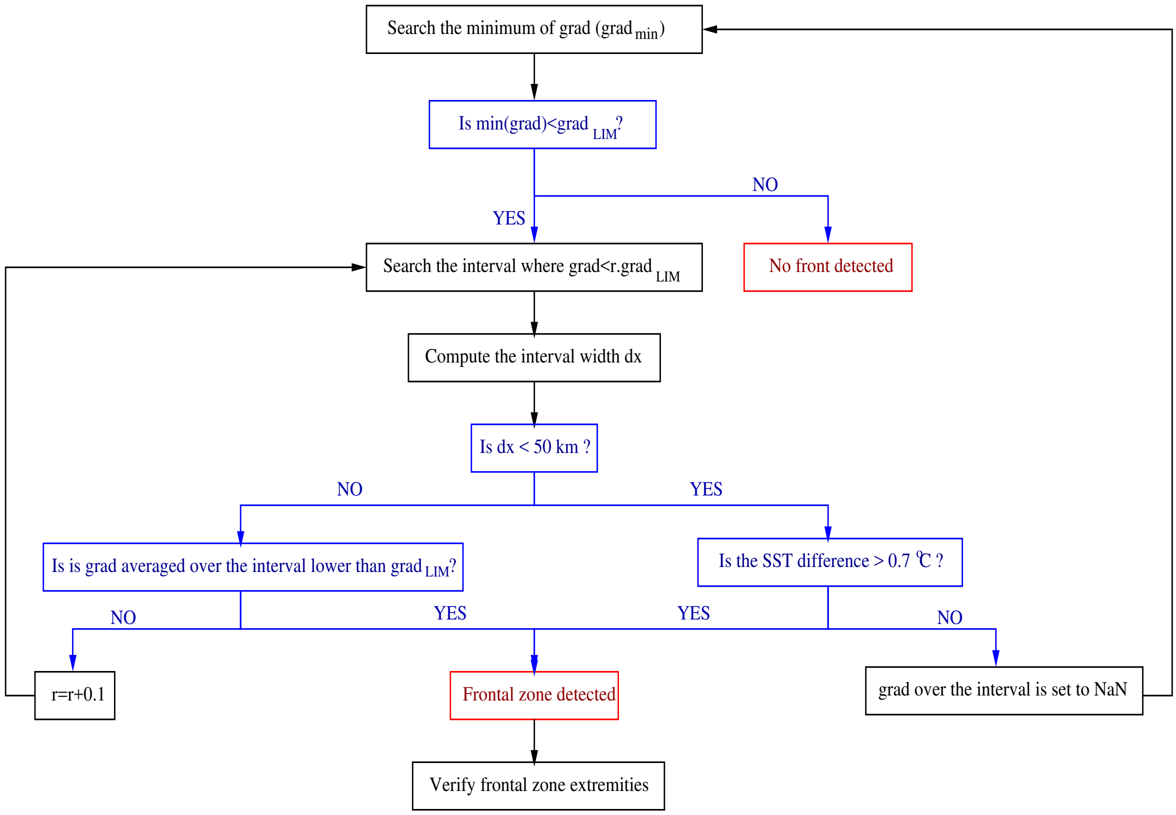

Figure A1. Scheme of the frontal zone identification from the smoothed SST profile.

At this step, the "frontal zone" identified corresponds to the interval around $grad_{min}$ where the mean $grad$ is below a threshold ($grad_{LIM}$ if $dx \geqslant 50$ km, and $\frac{0.7}{dx}$ if $dx < 50$ km). Note that this threshold is in any case lower than $grad_{LIM}$. The value of $grad_{LIM}$ corresponds to a strong cross-shore $grad$ for the HCS, it is negative enough to make sure that the interval is not too wide and includes too weak values of $grad$ near its extremities. However, x_1 and x_2 may need to be adjusted so that they actually delimit the strong $grad$ extension. This is necessary for two typical cases. First, when $grad$ is weak ($grad_{min} > -0.025$ °C km^{-1}, e.g., Figure A2a–c), the threshold is sometimes too low and the interval does not include all the area of strong $grad$. In this case, the frontal zone should be widened; this represents ∼2% of the analyzed maps. Second, when the peak around $grad_{min}$ is asymmetric (e.g., Figure A2d–f), the frontal zone should be reduced on one side, so that the interval only includes the strongest values of $grad$. This case corresponds to ∼10% of the analyzed maps. To adjust x_1 and x_2, the algorithm first analyzes whether the frontal zone should be widened. $grad$ is averaged over $\left[x_1 - \frac{dx}{2}, x_1\right]$ and over $\left[x_2, x_2 + \frac{dx}{2}\right]$. If one of these values is lower than $\frac{1}{3}grad_{min}$, the front is widened. To widen the frontal zone, $grad$ is smoothed using a running mean of size dx. The frontal zone is now determined as the interval where dx-smoothed $grad$ is lower than 30% of its minimum value. The algorithm also evaluates the peak symmetry by averaging $grad$ over $\left[x_1, x_1 + \frac{dx}{2}\right]$ and over $\left[x_1 + \frac{dx}{2}, x_2\right]$. If the difference between the two averages is larger than 40% of the peak intensity ($grad_{min} - \frac{grad(x_1)+grad(x_2)}{2}$), then the interval is reduced on the interval side with the weakest averaged $grad$. To reduce the frontal zone, $grad$ is smoothed using a running mean of size $\frac{dx}{2}$. The interval extremity that needs to be reduced is now determined by the point where the $\frac{dx}{2}$-smoothed $grad$ is equal to 40% of the peak intensity. If necessary, the symmetry evaluation and front reduction step is repeated three times to make sure that the frontal zone is reduced sufficiently.

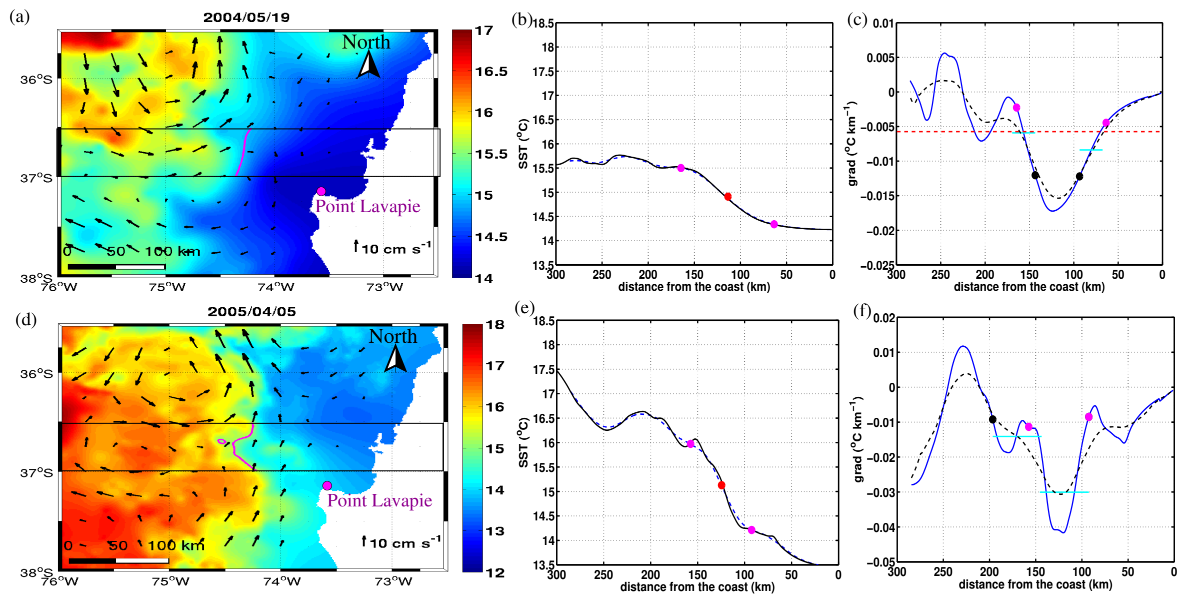

Figure A2. (**a**,**b**,**d**,**e**) Same as Figure 1a,b for: (**a**,**b**) 19 May 2004; and (**d**,**e**) 5 May 2005. (**c**–**f**) *grad* (in °C km^{-1}) with respect to the distance from the coast (blue line). Black (Magenta) points mark the frontal zone extremities x_1 and x_2 before (after, respectively) verifying whether the frontal zone should be widened and assessing the minimum peak symmetry. (**c**) Cyan lines correspond to the averaged values of *grad* over $\left[x_1 - \frac{dx}{2}, x_1\right]$ and over $\left[x_2, x_2 + \frac{dx}{2}\right]$. These values being lower than $\frac{1}{3}grad_{min}$ (red line), the frontal zone is widened using the dx-smoothed *grad* (dotted black line). (**f**) Note that the x_2 is unchanged before and after the verification. Cyan lines correspond to the averaged values of *grad* over $\left[x_1, x_1 + \frac{dx}{2}\right]$ and over $\left[x_1 + \frac{dx}{2}, x_2\right]$. The difference between these two values being larger than $\frac{40}{100}\left(grad_{min} - \frac{grad(x_1)+grad(x_2)}{2}\right)$, the frontal zone is reduced (offshore) using the $\frac{dx}{2}$-smoothed *grad* (dotted black line).

References

1. Lutjeharms, J.R.E.; Stockton, P.L. Kinematics of the upwelling front off southern Africa. *S. Afr. J. Mar. Sci.* **1987**, *5*, 35–49. [CrossRef]
2. Austin, J.A.; Barth, J.A. Variation in the position of the upwelling front on the Oregon shelf. *J. Geophys. Res.* **2002**, *107*, 3180. [CrossRef]
3. Peliz, A.; Rosa, T.L.; Santos, A.P.; Pissarra, J.L. Fronts, jets, and counter-flows in the Western Iberian upwelling system. *J. Mar. Syst.* **2002**, *35*, 61–77. [CrossRef]
4. Durski, S.M.; Allen, J.S. Finite-amplitude evolution of instabilities associated with the coastal upwelling front. *J. Phys. Oceanogr.* **2005**, *35*, 1606–1628. [CrossRef]
5. Strub, P.; James, C. Altimeter-derived variability of surface velocities in the California Current System: 2. Seasonal circulation and eddy statistics. *Deep Sea Res. Part II Top. Stud. Oceanogr.* **2000**, *47*, 831–870. [CrossRef]
6. Morales, C.E.; Gonzalez, H.E.; Hormazabal, S.E.; Yuras, G.; Letelier, J.; Castro, L.R. The distribution of chlorophyll-a and dominant planktonic components in the coastal transition zone off Concepcion, central Chile, during different oceanographic conditions. *Progr. Oceanogr.* **2007**, *75*, 452–469. [CrossRef]
7. Letelier, J.; Pizarro, O.; Nuñez, S. Seasonal variability of coastal upwelling and the upwelling front off central Chile. *J. Geophys. Res.* **2009**, *114*, C12009. [CrossRef]
8. Brink, K. Upwelling fronts: Implications and unknowns. *S. Afr. J. Mar. Sci.* **1987**, *5*, 3–9. [CrossRef]

9. Morales, C.E.; Hormazabal, S.E.; Correa-Ramirez, O.; Pizarro, O.; Silva, N.; Fernandez, C.; Anabalon, V.; Torreblanca, M. Mesoscale variability and nutrient-phytoplankton distributions off central-southern Chile during the upwelling season: The influence of mesoscale eddies. *Progr. Oceanogr.* **2012**, *104*, 17–29. [CrossRef]
10. Menschel, E.; Gonzalez, H.E.; Giesecke, R. Coastal-oceanic distribution gradient of coccolithophores and their role in the carbonate flux of the upwelling system off Concepcion, Chile (36°S). *J. Plankton Res.* **2016**, *38*, 798–817. [CrossRef]
11. Tiedemann, M.; Brehmer, P. Larval fish assemblages across an upwelling front: Indication for active and passive retention. *Estuar. Coast. Shelf Sci.* **2017**, *187*, 118–133. [CrossRef]
12. Demarcq, H.; Barlow, R.G.; Shillington, F.A. Climatology and variability of sea surface temperature and surface chlorophyll in the Benguela and Agulhas ecosystems as observed by satellite imagery. *Afr. J. Mar. Sci.* **2003**, *25*, 363–372. [CrossRef]
13. Sobarzo, M.; Bravo, L.; Donoso, D.; Garcés-Vargas, J.; Schneider, W. Coastal upwelling and seasonal cycles that influence the water column over the continental shelf off central Chile. *Progr. Oceanogr.* **2007**, *75*, 363–382. [CrossRef]
14. Morales, C.E.; Anabalon, V.; Bento, J.P.; Hormazabal, S.; Cornejo, M.; Correa-Ramirez, M.A.; Silva, N. Front-eddy influence on water column properties, phytoplankton community structure, and cross-shelf exchange of diatom taxa in the shelf-slope area off Concepcion (36–37°S). *J. Geophys. Res. Ocean.* **2017**, *122*, 8944–8965. [CrossRef]
15. Canny, J. A computational approach to edge detection. *IEEE Trans. Pattern Anal. Mach. Intell.* **1986**, *8*, 679–698. [CrossRef] [PubMed]
16. Cayula, J.F.; Cornillon, P. Edge detection algorithm for SST images. *J. Atmos. Ocean. Technol.* **1992**, *9*, 67–80. [CrossRef]
17. Pozo Vázquez, D.; Atae-Allah, C.; Luque Escamilla, P.L. Entropic approach to edge-detection for SST images. *J. Atmos. Ocean. Technol.* **1999**, *16*, 970–979. [CrossRef]
18. Torres, J.A.; Guindos, F.; Peralta, M.; Cantón, M. Competitive neural-net-based system for the automatic detection of oceanic mesoscalar structures on AVHRR scenes. *IEEE Trans. Geosci. Remote Sens.* **2003**, *41*, 845–852. [CrossRef]
19. Castelao, R.M.; Mavor, T.P.; Barth, J.A.; Breaker, L.C. Sea surface temperature fronts in the California Current System from geostationary satellite observations. *J. Geophys. Res.* **2006**, *111*, C09026. [CrossRef]
20. Belkin, I.; O'Reilly, J. An algorithm for oceanic front detection in chlorophyll and SST satellite imagery. *J. Mar. Syst.* **2009**, *78*, 319–326. [CrossRef]
21. Nieto, K.; Demarcq, H.; McClatchie, S. Mesoscale frontal structures in the Canary Upwelling System: New front and filament detection algorithms applied to spatial and temporal patters. *Remote Sens. Environ.* **2012**, *123*, 339–346. [CrossRef]
22. Cayula, J.F.; Cornillon, P. Multi-image edge detection for SST images. *J. Atmos. Ocean. Technol.* **1995**, *12*, 821–829. [CrossRef]
23. Diehl, S.F.; Budd, J.W.; Ullman, D.; Cayula, J.F. Geographic window sizes applied to remote sensing sea surface temperature front detection. *J. Atmos. Ocean. Technol.* **2002**, *19*, 1105–1113. [CrossRef]
24. Hormazabal, S.; Shaffer, G.; Letelier, J.; Ulloa, O. Local and remote forcing of Sea Surface Temperature in the coastal upwelling system off Chile. *J. Geophys. Res. Ocean.* **2001**, *106*, 16657–16671. [CrossRef]
25. Sobarzo, M.; Bravo, L.; Donoso, D.; Garces-Vargas, J.; Schneider, W. Coastal upwelling and seasonal cycles that influence the water column over the continental shelf off central Chile. *Prog. Oceanogr.* **2007**, *75*, 363–383. [CrossRef]
26. Renault, L.; Dewitte, B.; Falvey, M.; Garreaud, R.; Echevin, V.; Bonjean, F. Impact of atmospheric coastal jet off central Chile on sea surface temperature from satellite observations (2000–2007). *J. Geophys. Res.* **2009**, *114*, C08006. [CrossRef]
27. Aguirre, C.; Garreaud, R.D.; Rutllant, J.A. Surface ocean response to synoptic-scale variability in wind stress and heat fluxes off south-central Chile. *Dyn. Atmos. Ocean.* **2013**, *65*, 64–85. [CrossRef]
28. Leth, O.; Middleton, J.F. A numerical study of the upwelling circulation off central Chile: Effects of remote oceanic forcing. *J. Geophys. Res.* **2006**, *111*, C12003. [CrossRef]
29. Rutllant, J.A.; Masotti, I.; Calderón, J.; Vega, S.A. A comparison of spring coastal upwelling off central Chile at the extremes of the 1996–1997 ENSO cycle. *Cont. Shelf Res.* **2004**, *24*, 773–787. [CrossRef]

30. Colas, F.; Capet, X.; McWilliams, J.; Shchepetkin, A. 1997–1998 El Niño off Peru: A numerical study. *Prog. Oceanogr.* **2008**, *79*, 138–15. [CrossRef]
31. Aguirre, C.; Pizarro, O.; Strub, P.; Garreaud, R.; Barth, J. Seasonal dynamics of the near-surface alongshore flow off Central Chile. *J. Geophys. Res.* **2012**, *117*, C01006. [CrossRef]
32. Leth, O.; Middleton, J.F. A mechanism for enhanced upwelling off central Chile: Eddy advection. *J. Geophys. Res.* **2004**, *109*, C1202. [CrossRef]
33. Mesias, J.M.; Matano, R.P.; Strub, P.T. Dynamical analysis of the upwelling circulation off central Chile. *J. Geophys. Res.* **2003**, *108*, 3085. [CrossRef]
34. Wang, Y.; Castelao, R.M.; Yuan, Y. Seasonal variability of alongshore winds and sea surface temperature fronts in Eastern Boundary Current Systems. *J. Geophys. Res. Ocean.* **2015**, *120*, 2385–2400. [CrossRef]
35. SERNAPESCA. *Anuario Estadístico de Pesca 2006*; Ministerio de Economia, Fomento y Turismo: Santiago, Chile, 2006.
36. Physical Oceanography Distributed Active Archive Center. *JPL MUR MEaSUREs Project. 2015. GHRSST Level 4 MUR Global Foundation Sea Surface Temperature Analysis (v4.1). Version 4.1.*; Physical Oceanography Distributed Active Archive Center: Pasadena, CA, USA, 2015. [CrossRef]
37. Pujol, M.I.; Faugère, Y.; Taburet, G.; Dupuy, S.; Pelloquin, C.; Ablain, M.; Picot, N. DUACS DT2014: The new multi-mission altimeter data set reprocessed over 20 years. *Ocean Sci.* **2016**, *12*, 1067–1090. [CrossRef]
38. Bentamy, A.; Grodsky, S.; Carton, J.; Croizé-Fillon, D.; Chapron, B. Matching ASCAT and QuikSCAT winds. *J. Geophys. Res.* **2012**, *117*, C02011. [CrossRef]
39. Desbiolles, F.; Bentamy, A.; Blanke, B.; Roy, C.; Mestas-Nunez, A.; Grodsky, S.; Herbette, S.; Cambon, G.; Maes, C. Two decades [1992–2012] of surface wind analyses based on satellite scatterometer observations. *J. Mar. Syst.* **2017**, *168*, 38–56. [CrossRef]
40. National Oceanography Centre, Southampton, UK. NOCS Surface Flux Dataset v2.0. 2008. Available online: http://rda.ucar.edu/datasets/ds260.3/ (accessed on 24 January 2018).
41. Berry, D.I.; Kent, E.C. Air-sea fluxes from ICOADS: The construction of a new gridded dataset with uncertainty estimates. *Int. J. Climatol.* **2011**, *31*, 987–1001. [CrossRef]
42. NOAA. Cold and Warm Episodes by Season. 2018. Available online: http://origin.cpc.ncep.noaa.gov/products/analysis_monitoring/ensostuff/ONI_v5.php (accessed on 08 April 2018).
43. Schneider, W.; Donoso, D.; Garcés-Vargas, J.; Escribano, R. Water-column cooling and sea surface salinity increase in the upwelling region off Central-South Chile driven by a poleward displacement of the South Pacific High. *Prog. Oceanogr.* **2017**, *151*, 38–48. [CrossRef]
44. Morales, C.E.; Hormazabal, S.; Andrade, I.; Correa-Ramirez, M.A. Time-space variability of chlorophyll-a and associated physical variables within the region off central-southern Chile. *Remote Sens.* **2013**, *5*, 5550–5571. [CrossRef]
45. Castelao, R.M.; Barth, J.A. The role of wind stress curl in jet separation at a cape. *J. Phys. Oceanogr.* **2007**, *37*, 2652–2671. [CrossRef]
46. Kelly, K.A.; Caruso, M.J.; Austin, J.A. Wind-forced variations in sea surface height in the northeast Pacific ocean. *J. Phys. Oceanogr.* **1993**, *23*, 2392–2411. [CrossRef]
47. Lorenzo, E.D. Seasonal dynamics of the surface circulation in the Southern California Current System. *Deep Sea Res. Part II Top. Stud. Oceanogr.* **2003**, *50*, 2371–2388. [CrossRef]
48. Barth, J.A.; Pierce, S.D.; Cowles, T.J. Mesoscale structure and its seasonal evolution in the northern California Current System. *Deep Sea Res. Part II Top. Stud. Oceanogr.* **2005**, *52*, 5–28. [CrossRef]
49. Lynn, R.J.; Bograd, S.J.; Chereskin, T.K.; Huyer, A. Seasonal renewal of the California Current: The spring transition off California. *J. Geophys. Res. Ocean.* **2003**, *108*, 3279. [CrossRef]
50. Belmadani, A.; Echevin, V.; Codron, F.; Takahashi, K.; Junquas, C. What dynamics drive future winds scenarios off Peru and Chile? *Clim. Dyn.* **2014**, *43*, 1893–1914. [CrossRef]
51. Bakun, A.; Weeks, S.J. The marine ecosystem off Peru: What are the secrets of its fishery productivity and what might its future hold? *Prog. Oceanogr.* **2008**, *79*, 290–299. [CrossRef]
52. Goubanova, K.; Echevin, V.; Dewitte, B.; Codron, F.; Takahashi, K.; Terray, P.; Vrac, M. Statistical downscaling of sea-surface wind over the Peru–Chile upwelling region: Diagnosing the impact of climate change from the IPSL-CM4 model. *Clim. Dyn.* **2011**, *36*, 1365–1378. [CrossRef]

53. Sydeman, W.; García-Reyes, M.; Schoeman, D.S.; Rykaczewski, R.R.; Thompson, S.A.; Black, B.A.; Bograd, S.J. Climate change and wind intensification in coastal upwelling ecosystems. *Science* **2014**, *345*, 77–80. [CrossRef] [PubMed]
54. Marchesiello, P.; McWilliams, J.C.; Shchepetkin, A. Equilibrium structure and dynamics of the California current system. *J. Phys. Oceanogr.* **2003**, *33*, 753–783. [CrossRef]
55. Belmadani, A.; Echevin, V.; Dewitte, B.; Colas, F. Equatorially forced intraseasonal propagations along the Peru-Chile coast and their relation with the nearshore eddy activity in 1992–2000: A modeling study. *J. Geophys. Res.* **2012**, *117*, C04025. [CrossRef]
56. Pelegrí, J.; Arístegui, J.; Cana, L.; González-Dávila, M.; Hernández-Guerra, A.; Hernández-León, S.; Marrero-Díaz, A.; Montero, M.; Sangrà, P.; Santana-Casiano, M. Coupling between the open ocean and the coastal upwelling region off northwest Africa: Water recirculation and offshore pumping of organic matter. *J. Mar. Syst.* **2005**, *54*, 3–37. [CrossRef]
57. Capet, X.; McWilliams, J.C.; Molemaker, M.J.; Shchepetkin, A.F. Mesoscale to submesoscale transition in the California Current System. Part II: Frontal processes. *J. Phys. Oceanogr.* **2008**, *38*, 44–64. [CrossRef]
58. Hösen, E.; Möller, J.; Jochumsen, K.; Quadfasel, D. Scales and properties of cold filaments in the Benguela upwelling system off Lüderitz. *J. Geophys. Res. Ocean.* **2016**, *121*, 1896–1913. [CrossRef]
59. Colas, F.; McWilliams, J.C.; Capet, X.; Kurian, J. Heat balance and eddies in the Peru-Chile current system. *Clim. Dyn.* **2012**, *39*, 509–529. [CrossRef]
60. Castelao, R.M.; Wang, Y. Wind-driven variability in sea surface temperature front distribution in the California Current System. *J. Geophys. Res. Ocean.* **2014**, *119*, 1861–1875. [CrossRef]
61. Vazquez-Cuervo, J.; Torres, H.S.; Menemenlis, D.; Chin, T.; Armstrong, E.M. Relationship between SST gradients and upwelling off Peru and Chile: Model/satellite data analysis. *Int. J. Remote Sens.* **2017**, *38*, 6599–6622. [CrossRef]
62. Kahru, M.; Di Lorenzo, E.; Manzano-Sarabia, M.; Mitchell, B. Spatial and temporal statistics of Sea Surface Temperature and chlorophyll fronts in the California Current. *J. Plankton Res.* **2012**, *34*, 749–760. [CrossRef]
63. Capet, X.; McWilliams, J.C.; Molemaker, M.J.; Shchepetkin, A.F. Mesoscale to submesoscale transition in the California Current System. Part I: Flow structure, eddy flux, and observational tests. *J. Phys. Oceanogr.* **2008**, *38*, 29–43. [CrossRef]
64. Mahadevan, A. The impact of submesoscale physics on primary productivity of plankton. *Ann. Rev. Mar. Sci.* **2016**, *8*, 161–184. [CrossRef] [PubMed]
65. McWilliams, J.C. Submesoscale currents in the ocean. *Proc. R. Soc. A* **2016**, *472*, 20160117. [CrossRef] [PubMed]
66. D'Asaro, E.; Lee, C.; Rainville, L.; Harcourt, R.; Thomas, L. Enhanced turbulence and energy dissipation at ocean fronts. *Science* **2011**, *15*, 318–322. [CrossRef] [PubMed]
67. Johnston, T.; Rudnick, D.L.; Pallas-Sanz, E. Elevated mixing at a front. *J. Geophys. Res.* **2011**, *116*, C11033. [CrossRef]
68. Merlivat, L.; Davila, M.G.; Caniaux, G.; Boutin, J.; Reverdin, G. Mesoscale and diel to monthly variability of CO_2 and carbon fluxes at the ocean surface in the northeastern Atlantic. *J. Geophys. Res.* **2009**, *114*, C03010. [CrossRef]
69. Ferrari, R. A frontal challenge for climate models. *Science* **2011**, *332*, 316–317. [CrossRef] [PubMed]
70. Köhn, E.E.; Thomsen, S.; Arévalo-Martínez, D.L.; Kanzow, T. Submesoscale CO_2 variability across an upwelling front off Peru. *Ocean Sci.* **2017**, *13*, 1017–1033. [CrossRef]
71. Lévy, M.; Franks, P.; Martin, A.P.; Rivière, P. Bringing physics to life at the submesoscale. *J. Geophys. Res.* **2012**, *39*, L14602. [CrossRef]
72. Stukel, M.R.; Aluwihare, L.I.; Barbeau, K.A.; Chekalyuk, A.M.; Goericke, R.; Miller, A.J.; Ohman, M.D.; Ruacho, A.; Song, H.; Stephens, B.M.; et al. Mesoscale ocean fronts enhance carbon export due to gravitational sinking and subduction. *PNAS* **2017**, *114*, 1252–1257. [CrossRef] [PubMed]
73. Thomsen, S.; Kanzow, T.; Colas, F.; Echevin, V.; Krahmann, G.; Engel, A. Do submesoscale frontal processes ventilate the oxygen minimum zone off Peru? *Geophys. Res. Lett.* **2016**, *43*, 8133–8142. [CrossRef]
74. Li, Q.P.; Franks, P.J.S.; Ohman, M.; Landry, M.R. Enhanced nitrate fluxes and biological processes at a frontal zone in the Southern California Current System. *J. Plankton Res.* **2012**, *34*, 790–801. [CrossRef]

75. Taylor, A.G.; Goericke, R.; Landry, M.R.; Selph, K.E.; Wick, D.A.; Roadman, M.J. Sharp gradients in phytoplankton community structure across a frontal zone in the California Current Ecosystem. *J. Plankton Res.* **2012**, *34*, 778–789. [CrossRef]
76. Ohman, M.D.; Powell, J.R.; Picheral, M.; Jensen, D. Mesozooplankton and particulate matter responses to a deep-water frontal system in the southern California Current System. *J. Plankton Res.* **2012**, *34*, 815–827. [CrossRef]
77. Krause, J.W.; Brzezinski, M.A.; Goericke, R.; Landry, M.R.; Ohman, M.D.; Stukel, M.R.; Taylor, A.G. Variability in diatom contributions to biomass, organic matter production and export across a frontal gradient in the California Current Ecosystem. *J. Geophys. Res. Ocean.* **2015**, *120*, 1032–1047. [CrossRef]
78. Böttjer, D.; Morales, C.E. Nanoplanktonic assemblages in the upwelling area off Concepción (∼36°S), central Chile: Abundance, biomass, and grazing potential during the annual cycle. *Progr. Oceanogr.* **2007**, *75*, 415–434. [CrossRef]
79. Castro, L.R.; Troncoso, V.A.; Figueroa, D.R. Fine-scale vertical distribution of coastal and offshore copepods in the Golfo de Arauco, central Chile, during the upwelling season. *Prog. Oceanogr.* **2007**, *75*, 486–500. [CrossRef]